

Representation of Rossby wave propagation and its effect on the teleconnection between the Indian summer monsoon and extratropical rainfall in the Met Office Unified Model

Xinxin Tang

Ocean University of China

Jianping Li (✉ ljp@ouc.edu.cn)

Ocean University of China <https://orcid.org/0000-0003-0625-1575>

Huqiang Zhang

Australian Bureau of Meteorology

Sen Zhao

University of Hawai'i at Manoa

Research Article

Keywords: Rossby wave, Indian summer monsoon rainfall, Interhemispheric teleconnection, Meridional wind, Met Office Unified Model

Posted Date: May 28th, 2021

DOI: <https://doi.org/10.21203/rs.3.rs-255748/v1>

License: © ⓘ This work is licensed under a Creative Commons Attribution 4.0 International License.

[Read Full License](#)

Version of Record: A version of this preprint was published at Climate Dynamics on September 13th, 2021. See the published version at <https://doi.org/10.1007/s00382-021-05940-4>.

Abstract

25

26 Compared with Global Atmosphere 6 (GA6) of the UK Met Office Unified Model
27 (UM), the dry bias over the Indian monsoon region in Global Atmosphere 7 (GA7) is
28 significantly reduced. However, the physical processes controlling how this reduced
29 dry bias in India influences rainfall teleconnections in the extratropics remain unclear.
30 Thus, in this study, we use Rossby wave tracing in a horizontally nonuniform
31 background flow to investigate how the improved simulation of monsoon rainfall in
32 GA7 compared with GA6 affects extratropical rainfall teleconnections. We find that
33 wave rays emanating from the upper troposphere in the Indian monsoon region first
34 propagate westward, then divide into the Northern Hemisphere (NH) subtropical
35 westerlies over Asia and the Southern Hemisphere (SH) subtropical westerlies. The
36 wave ray trajectories in GA7 in years of strong Indian summer monsoon rainfall (ISMR)
37 are closer to observations than those in GA6. We also find that the upper tropospheric
38 meridional winds over the South Asian monsoon region and western Tibetan Plateau
39 are much better simulated in GA7 than in GA6 owing to the improvement of ISMR
40 and South Asian High (SAH), which leads to a more realistic simulation of the wave
41 rays in GA7. The better simulated circulation teleconnections in GA7 then modulate
42 the vertical motion and moisture transport, and hence affect extratropical rainfall
43 anomalies in the NH and SH. This paper provides new insights for the assessment of
44 tropical–extratropical teleconnections in models.

45 **1. Introduction**

46 The Unified Model (UM) is the atmospheric component of the numerical
47 modelling system created by the UK Met Office (UKMO) for both weather and climate
48 applications (<https://www.metoffice.gov.uk/research/modelling-systems>). It is widely
49 used by many organizations and agencies around the world, particularly in the
50 Australian–Asian region, including Australia, India, Korea, and the Philippines
51 ([https://www.metoffice.gov.uk/research/approach/collaboration/unified-](https://www.metoffice.gov.uk/research/approach/collaboration/unified-model/partnership)
52 [model/partnership](https://www.metoffice.gov.uk/research/approach/collaboration/unified-model/partnership)). Two versions of the UM, namely the UM Global Atmosphere 6
53 (GA6) and 7 (GA7) are being used by the UK and Australia to contribute to the
54 Intergovernmental Panel on Climate Change (IPCC) Coupled Model Intercomparison
55 Project (CMIP6) (Hirst, 2015; Walters et al., 2019) and in their operational seasonal
56 forecast systems (MacLachlan et al., 2015; Hudson et al., 2017). As a result, assessing
57 the performance of the UM GA in the Australian–Asian monsoon region has been an
58 important topic of past research.

59 As noted in previous UM assessments (Walters et al., 2014, 2017, 2019), the UM
60 has a climatological rainfall deficit over the Indian subcontinent. However, the
61 simulation of Indian summer monsoon rainfall (ISMR) within a given UM
62 configuration was shown to improve when the model resolution was increased (Prakash
63 et al., 2016; Jin et al., 2019). In a recent UM GA assessment study, Jin et al. (2019)
64 showed that the area-averaged summer monsoon rainfall over the Indian subcontinent
65 (70°–90°E, 5°–25°N) was significantly increased in GA7 compared with GA6.
66 Furthermore, the increased ISMR in GA7 with N216 resolution improved monsoon–

67 desert rainfall teleconnections and generated more realistic remote rainfall correlation
68 patterns in the Australian–Asian region. Part of the teleconnection patterns showed
69 similarity with Rossby wave propagation from the tropics into the middle and high
70 latitudes. However, as acknowledged by the authors, the underlying physical and
71 dynamic processes supporting these improved rainfall teleconnection patterns and the
72 increased ISMR in the simulations was not fully explored (Jin et al., 2019). The major
73 goal of this study is therefore to further investigate how the simulation of Indian
74 monsoon rainfall in GA6 and GA7 (Walters et al., 2017, 2019) affects the representation
75 of tropical–extratropical rainfall teleconnections, and the nature of the underlying
76 physical and dynamical processes. This analysis will also help to better understand the
77 simulated current and future climate in these models in preparation for CMIP6.

78 The extratropical atmospheric response to tropical localized forcing is well
79 established in both the Northern Hemisphere (NH) (Nitta, 1987; Hoskins and Rodwell,
80 1995; Rodwell and Hoskins, 1996; Kripalani et al., 1997; Wang et al., 2001; Ding and
81 Wang, 2005, 2007; Lin, 2009) and the Southern Hemisphere (SH) (Wang et al., 2001;
82 Lin, 2009; Lee et al., 2013; Liu and Wang, 2013; Zhao et al., 2019). Several summer
83 teleconnection patterns in the NH associated with tropical monsoons have been
84 investigated, including the Pacific–Japan pattern (Nitta, 1987, 1989), the East Asia–
85 Pacific pattern (Huang and Lu, 1987, Huang and Sun, 1992), the circumglobal
86 teleconnection pattern (Ding and Wang, 2005; Ding et al., 2011), the “silk road”
87 pattern in the 200 hPa meridional velocity (Lu et al., 2002; Enomoto et al., 2003), the
88 Indo–Asian–Pacific pattern (Li et al., 2011; Li et al., 2013), and the North Atlantic–

89 Eurasian teleconnection (Li et al., 2013; Li and Ruan, 2018; Li et al., 2019). In
90 addition, the circulation variability in the SH induced by tropical heating was the topic
91 of several studies, including the Pacific–South America pattern (Karoly, 1989), the
92 South Africa–midlatitude pattern and the Maritime Continent–subtropical Australian
93 pattern (Zhao et al., 2019). The mechanism proposed for these tropical–extratropical
94 teleconnections is Rossby wave propagation and energy dispersion from localized
95 tropical heating anomalies (Hoskins and Karoly, 1981; Branstator, 1983; Li and Nathan,
96 1994). As some theoretical studies have proved (e.g., Hoskins and Karoly, 1981;
97 Simmons, 1982; Branstator, 1983; Lau and Lim, 1984; Branstator, 1985), these
98 anomalies excite stable two-dimensional Rossby waves, thereby dispersing energy to
99 remote regions of the globe.

100 These wave energy dispersion pathways can be well represented by the “great
101 circle” ray trajectory (Hoskins and Karoly, 1981). However, in models with a zonally
102 varying or zonally symmetric basic flow, stationary waves can only propagate in the
103 westerlies and cannot cross the critical latitude (i.e., the zero zonal wind speed line;
104 Hoskins and Karoly, 1981; Branstator, 1983). As there is a strong easterly wind
105 prevailing at upper levels of the atmosphere in the Indian monsoon region during boreal
106 summer, the Rossby waves are evanescent and cannot propagate into the SH in these
107 kinds of models. In reality, however, the Asian monsoon system has a strong meridional
108 circulation and its meridional wind cannot be neglected, compared with the zonal wind.
109 Schneider and Watterson (1984) and Zhang et al. (1996) proved theoretically and
110 numerically that the Hadley circulation allows Rossby waves to propagate from one

111 hemisphere to another via the easterly winds.

112 Li and Li (2012) further considered the barotropic, non-divergent vorticity
113 equation in a horizontally nonuniform basic flow, and found that steady Rossby waves
114 can propagate in the easterlies when supported by the meridional wind. On the basis of
115 the theory of Li and Li (2012), further research has also demonstrated that stationary
116 waves originating from the tropical easterlies can propagate across the equator (Li et
117 al., 2015; Zhao et al., 2015, 2019).

118 Another physical mechanism behind cross-equatorial easterly teleconnections was
119 proposed by Sardeshmukh and Hoskins (1988). They suggested that the equatorial
120 forcing in the easterly winds induces a Rossby wave source in the subtropical westerlies
121 caused by the advection of vorticity by the perturbed divergent flow. However, the
122 divergent wind is much evident over upper tropospheric maritime continent during
123 boreal summer and cannot simply explain the dynamical process of interhemispheric
124 teleconnections associated with ISMR. In this study, therefore, stationary Rossby wave
125 ray tracing is employed to investigate rainfall teleconnections simulated in the UM
126 models.

127 The main focus of this study is to examine how the improved simulation of ISMR
128 in GA7 compared with GA6 influences extratropical precipitation over the Australian–
129 Asian monsoon region, and the nature of the underlying physical and dynamical
130 mechanisms. We pay particular attention to exploring the signature of stationary Rossby
131 wave energy dispersion in a horizontally nonuniform basic flow within the simulations.

132 The paper is organized as follows. In Section 2, the model, data, and methodology

133 used in this study are introduced. Section 3 is used to assess the rainfall simulations in
134 GA6 and GA7. Section 4 describes the circulation anomalies in the SH and NH
135 associated with ISMR and analyzes their influence on the extratropical rainfall.
136 Section 5 presents the trajectories obtained via Rossby wave ray tracing and discusses
137 the role of meridional wind ducts related to ISMR and South Asian High (SAH).
138 Section 6 contains a summary and discussion.

139 **2. Model, data and methodology**

140 **2.1 Model**

141 In this paper, we use monthly precipitation, winds, and geopotential height data
142 obtained from numerical experiments with the UM GA6 and GA7 (Walters et al., 2017,
143 2019) using a horizontal resolution of 60 km (N216 grid). We used atmosphere-only
144 UM GA simulations by forcing the model with daily observed sea surface temperature
145 (SST) and sea-ice conditions for the period 1982–2008, as in Walters et al. (2017, 2019)
146 and Jin et al. (2019).

147 Detailed descriptions of the UM GA6 and GA7 configurations have been provided
148 in several publications (Walters et al., 2017, 2019; Jin et al., 2019), and here we list
149 only some of the key features that are relevant to this study. The GA6 solves the non-
150 hydrostatic, fully compressible, deep-atmosphere equations of motion with a semi-
151 implicit semi-Lagrangian formulation and ENDGame dynamical core (Wood et al.,
152 2014). It uses extensively modified microphysics based on Wilson and Ballard (1999)
153 and a revised version of the convection scheme of Gregory and Rowntree (1990) that
154 includes downdrafts (Gregory and Allen, 1991) and convective momentum transport.

155 As pointed out by Walter et al. (2019) and Jin et al. (2019), GA7 includes further
156 developments of the model's microphysics scheme and incremental improvements to
157 the implementation of the dynamical core. It includes improved treatment of gaseous
158 absorption in the radiation scheme, improvements to the treatment of warm rain and ice
159 clouds, and revisions to the model's convection scheme to improve the fidelity of the
160 simulation of rainfall. These developments lead to large reductions in four critical
161 model errors: rainfall deficits over India during the South Asian monsoon, temperature
162 and humidity biases in the tropical tropopause layer, deficiencies in the model's
163 numerical conservation, and surface flux biases over the Southern Ocean (Walters et al.,
164 2019).

165 **2.2 Observational data**

166 In order to evaluate the simulated Indian Monsoon precipitation, we use monthly
167 precipitation from the Global Precipitation Climatology Project (GPCP; Adler et al.,
168 2003) for the period 1982–2008. Furthermore, the horizontal winds from ERA-Interim
169 reanalysis (Dee et al., 2011) are used for the Rossby wave ray tracing, whilst the
170 geopotential height from ERA-Interim reanalysis data with a resolution of 2.5°
171 longitude by 2.5° latitude for the period 1982–2008 is used to evaluate the monsoon
172 circulation.

173 The indices used in this study are as follows. The Niño-3.4 index obtained from
174 the Climate Prediction Center (<http://www.cpc.ncep.noaa.gov/data/indices/>), defined as
175 the area-averaged SST anomalies over 5°S – 5°N , 170° – 120°W , is used to quantify the
176 El Niño Southern Oscillation (ENSO). The Indian Ocean Dipole (IOD) Mode index

177 (DMI) obtained from National Oceanic and Atmospheric Administration (NOAA)
178 (http://www.esrl.noaa.gov/psd/gcos_wgsp/Timeseries/DMI/) is defined as the
179 difference in the SST anomaly between the tropical western Indian Ocean (10°S – 10°N ,
180 50° – 70°E) and the southeastern Indian Ocean (10°S – 0°N , 90° – 110°E ; Saji et al., 1999).
181 To quantify the Indian summer monsoon, many indices based on the precipitation, OLR
182 or 850 hPa wind anomalies have been used in the literature (Wang et al., 2001; Li and
183 Zeng, 2002, 2003, 2005; Ding and Wang, 2007). In this paper, in order to evaluate the
184 ISMR-dependent teleconnections in GA6 and GA7, we define the ISMR Index (ISMRI)
185 as the normalized area-averaged rainfall anomaly over the Indian subcontinent (5° –
186 25°N , 70° – 90°E), as in Jin et al. (2019). Furthermore, we define the ISMR as being
187 strong (weak) when the ISMRI is above (below) 0.75 (–0.75) considering both the
188 significance and the number of strong (weak) ISMR events. Furthermore, both the
189 strong and weak ISMR years selected in observation and GA7 are six years, and the
190 strong and weak ISMR years in GA6 are seven and six years, respectively. Note that by
191 choosing a larger domain covering the whole of the south Asian monsoon region, Jin et
192 al. (2019) showed that the agreement between GA7 simulations and observations was
193 much improved. We define the south Asian monsoon region as the area over 5° – 25°N ,
194 30° – 90°E .

195 **2.3 Partial correlation**

196 In our analysis, we use the first-order partial correlation coefficient (Anderson,
197 1984) to calculate the correlation between two time series, excluding the effect of one
198 other control variable as follows:

199
$$r_{ij \cdot k} = \frac{r_{ij} - r_{ik} \times r_{jk}}{\sqrt{(1 - r_{ik}^2) \times (1 - r_{jk}^2)}}, \quad (1)$$

200 where $r_{ij \cdot k}$ denotes the partial correlation of variables i and j , excluding the effect of
 201 k , r_{ij} refers to the linear correlation between variables i and j , r_{ik} refers to the linear
 202 correlation between variables i and k , and r_{jk} refers to the linear correlation between
 203 variables j and k .

204 The second-order partial correlation coefficient (Anderson, 1984), used to
 205 determine the correlation between two time series excluding the effect of two other
 206 control variables, is calculated as follows:

207
$$r_{ij \cdot kh} = \frac{r_{ij \cdot k} - r_{ih \cdot k} \times r_{jh \cdot k}}{\sqrt{(1 - r_{ih \cdot k}^2) \times (1 - r_{jh \cdot k}^2)}}, \quad (2)$$

208 where $r_{ij \cdot kh}$ denotes the partial correlation between variables i and j , excluding the
 209 signals of k and h , and $r_{ij \cdot k}$, $r_{ih \cdot k}$, and $r_{jh \cdot k}$ can be obtained from Eq. (1).

210 **2.4 Partial regression**

211 The partial regression is adopted to estimate how much of the variation of the
 212 response variable can be attributed exclusively to one set of factors, once the effect of
 213 the other set has been taken into account and controlled for. Specifically, the influences
 214 of the considered factors on the studied variables are eliminated the step by step. Let's
 215 take three independent variables X , X_1 , X_2 as an example, and Y be the dependent
 216 variable. Firstly, the effect of X_1 on y is removed by subtracting the regression of Y on
 217 X_1 . The regressed values of Y are assumed to follow certain distribution:

218
$$\tilde{Y}'(t) = aX1'(t) + a1, \quad (3)$$

219 primes represent departure from the mean state, a is the regression coefficient, and
 220 $a1$ is the intercept of linear regression. \tilde{Y}' indicates the linear contribution of $X1'$ on
 221 Y' . Then the effect of $X1$ on Y is eliminated by

222
$$Y'^*(t) = Y'(t) - \tilde{Y}'(t). \quad (4)$$

223 Y'^* is isolate from $X1$. Then the same way is used to remove the liner influence of $X2$
 224 on y . Linear contribution of $X2$ on Y'^* is

225
$$\tilde{Y}'^*(t) = bX2'(t) + b1, \quad (5)$$

226 where \tilde{Y}'^* indicates the regression of Y'^* on $X2'$. The linear influence of $X2$ can be
 227 excluded by

228
$$Y'^{**}(t) = Y'^*(t) - \tilde{Y}'^*(t). \quad (6)$$

229 In this case, the linear contributions of $X1$ and $X2$ on $Y'(t)$ are removed. The $\tilde{Y}'^{**}(t)$
 230 that is attributed exclusively to X takes the form of

231
$$\tilde{Y}'^{**}(t) = cX'(t) + c1, \quad (7)$$

232 in which c is the partial regression coefficient, and \tilde{Y}'^{**} is the partial regressed value
 233 by X' .

234 **2.5 Rossby wave theory in a nonuniform horizontal basic flow**

235 Rossby wave ray tracing theory describes the pathway of wave energy dispersion
 236 (Hoskins and Karoly, 1981, Li et al., 2015; Zhao et al., 2015, 2019) and has been widely
 237 used to explore atmospheric teleconnections. Thus, it is used in this study to reveal the
 238 dynamical link between ISMR and the extratropical climate. A linearized, spherical
 239 barotropic Rossby wave ray tracing model proposed by Li and Li (2012) and Li et al.

240 (2015) is employed to study steady, linear Rossby wave patterns in a nonuniform
 241 horizontal basic flow. According to Zhao et al. (2015, 2019), the dispersion relation of
 242 a barotropic Rossby wave is

$$243 \quad \omega = \bar{u}_M k + \bar{v}_M l + \frac{l \partial \bar{q} / \partial x - k \partial \bar{q} / \partial y}{K^2}, \quad (8)$$

244 where ω is the frequency, $(\bar{u}_M, \bar{v}_M) = (\bar{u}, \bar{v}) / \cos \varphi$ is the Mercator projection of the
 245 basic-state zonal and meridional winds, φ is the latitude, $q = 2\Omega \sin \varphi + \nabla^2 \bar{\Psi}$ is the
 246 basic-state absolute vorticity, Ω is the rotation rate of Earth, $\bar{\Psi}$ is the basic-state
 247 stream function, $K = \sqrt{k^2 + l^2}$ is the total wavenumber, and k and l are the zonal and
 248 meridional wavenumbers, respectively. The local group velocity $\mathbf{C}_g = (u_g, v_g)$ obtained
 249 from Eq. (8) takes the form (Li et al., 2015; Zhao et al., 2015)

$$250 \quad u_g = \bar{u}_M + [(k^2 - l^2) \partial \bar{q} / \partial y - 2kl \partial \bar{q} / \partial x] / K^4, \quad (9a)$$

$$251 \quad v_g = \bar{v}_M + [2kl \partial \bar{q} / \partial y + (k^2 - l^2) \partial \bar{q} / \partial x] / K^4. \quad (9b)$$

252 The wave ray trajectory is tangential to the group velocity (Lighthill, 1978). The
 253 wavenumbers k and l , which are determined by kinematic wave theory (Whitham, 1960;
 254 Shaman et al., 2012), vary with the position of the ray,

$$255 \quad \frac{d_g k}{dt} = -k \frac{\partial \bar{u}_M}{\partial x} - l \frac{\partial \bar{v}_M}{\partial x} + \frac{k \partial^2 \bar{q} / \partial y \partial x - k \partial^2 \bar{q} / \partial x^2}{K^2}, \quad (10a)$$

$$256 \quad \frac{d_g l}{dt} = -k \frac{\partial \bar{u}_M}{\partial y} - l \frac{\partial \bar{v}_M}{\partial y} + \frac{k \partial^2 \bar{q} / \partial y^2 - k \partial^2 \bar{q} / \partial x \partial y}{K^2}, \quad (10b)$$

257 where $d_g / dt = \partial / \partial t + \mathbf{C}_g \cdot \nabla$. For stationary waves ($\omega = 0$), the initial local
 258 meridional wavenumber l is determined from the dispersion relation Eq. (8) for each
 259 initial zonal wavenumber k and a given starting point. Then, the ray trajectory can be
 260 numerically integrated from Eqs (9) and (10). The integration was aborted when the
 261 local meridional wavelength was calculated as < 1000 km.

262 From Eqs. (9) and (10), it can be seen that the barotropic stationary Rossby wave
263 energy is dominated by the basic zonal flow, basic meridional flow, and absolute
264 vorticity gradient. Notably, the meridional basic flow plays an important role in the
265 dispersion of wave energy particularly over tropical monsoon region where meridional
266 wind can't be ignored compared with zonal wind. Furthermore, considering the wave
267 ray trajectory is sensitive to the background flow and the atmospheric circulation is
268 subject to multiple factors, it is necessary to extract the influence of heating anomalies
269 on the background flow by partial regression. In this paper, we considered the effects
270 of ENSO and IOD. The basic flow is divided into climatological and abnormal parts,
271 and abnormal wind is partial regressed onto the ISMRI to exclude the effects of ENSO
272 and IOD.

273 **3. Rainfall simulations in GA6 and GA7**

274 Many studies have reported that the tropical monsoons have consequences for
275 rainfall outside the tropics (Nitta, 1987; Hoskins and Rodwell, 1995; Rodwell and
276 Hoskins, 1996; Kripalani et al., 1997; Wang et al., 2001; Ding and Wang, 2005, 2007;
277 Lin, 2009; Lee et al., 2013; Liu and Wang, 2013; Zhao et al., 2019). Since the
278 relationship between ISMR and regional rainfall may be modulated by the influence of
279 tropical SSTs, the impacts of some known tropical SST signals on rainfall anomalies
280 are usually excluded first to better isolate the influence of ISMR on rainfall
281 teleconnections. In the study of Jin et al. (2019), they eliminated the effect of ENSO
282 when they investigated the correlation between the simulated ISMR and rainfall over

283 the Australian–Asian monsoon region in GA6 and GA7. Although they discussed the
284 likely influence of the IOD on rainfall anomalies in the Australian–Asian region (Ashok
285 et al., 2001; Zhao et al., 2014; Zhao and Zhang, 2016) in GA6 and GA7, their analysis
286 did not remove the effects of the IOD. In this study, we take both the IOD and ENSO
287 into account.

288 Figure 1 displays the correlations and partial correlations between the ISMRI and
289 the June–July–August (JJA) rainfall over the Australian–Asian monsoon region from
290 GPCP, GA6, and GA7, excluding the impacts of the IOD and ENSO. The partial
291 correlations bare close resemblance to the full correlations. Notably, the rainfall
292 anomalies in the SH particularly over southwest Australia are more evident in GPCP
293 after removing the impacts of ENSO and IOD indicating that the influence of ENSO,
294 IOD and ISMR on the SH rainfall teleconnections are relatively depended. Furthermore,
295 the rainfall teleconnections are in good agreement with the results of Jin et al. (2019;
296 cf. their Fig. 7). In the NH, a wave train-like rainfall teleconnection pattern (Wu, 2002,
297 2017; Kim et al., 2002), which shows positive correlations over Arabian Peninsula,
298 Northern China and Mongolia, and negative correlations over Central Asia and the
299 Korean Peninsula, is much better captured by GA7 (Figs. 1a, b, c), as reported in Jin et
300 al. (2019, cf. their Fig. 7). In addition, in the NH, the anomalous rainfall pattern
301 correlations between GA7 and observations for the full correlation and partial
302 correlation are 0.496 and 0.431, respectively, but is better than GA6, where the
303 correlation with observations are 0.329 and 0.255, respectively.

304 In the SH, negative correlations over the subtropical Indian Ocean and positive
305 correlations over tropical western Indian Ocean and southwest Australia and the nearby
306 Indian Ocean (Figs. 1a, d), are evident in observations, as also shown by Jin et al. (2019,
307 cf. their Fig. 7). The anomalous rainfall pattern correlation in the SH between GA7 and
308 observations for the full correlation and partial correlation are 0.251 and 0.068.
309 respectively, but is better and worse simulated in GA6, where the correlations with
310 observations are 0.155 and 0.26, respectively. The decrease in the partial correlation
311 between GA7 and observations is mainly owing to the different influences of ENSO
312 and IOD on the rainfall teleconnection magnitude in GA7 and observation. However,
313 according to the full correlation, the wave-train-like correlation pattern is still better
314 captured by GA7 (Figs.1b, c, d, e). Particularly, GA6 overestimated the positive
315 correlation over Australia and the overestimation is reduced in GA7 (Figs.1b, c, d, e).
316 Overall, the rainfall correlation between GA7 and observations over the Australian–
317 Asian domain (50°S–60°N, 30°–180°E) is still low at 0.31, but is better than GA6,
318 where the correlation with observations is 0.251. In addition, the rainfall
319 teleconnections in the NH are better simulated than that in the SH for both GA6 and
320 GA7. Moreover, we still have to point out that the rainfall correlations with the ISMRI
321 over ISM and northwest of ISM regions are poor simulated in both GA6 and GA7 which
322 need further investigation.

323 We further evaluate the ISMR intensity to help understand the fidelity of rainfall
324 teleconnections simulated in GA6 and GA7. Figure 2 shows the spatial distribution of
325 precipitation during years of strong and weak ISMR in observations, GA7, and GA6.

326 Rainfall deficits over the Indian subcontinent during years of strong ISMR are reduced
327 markedly in GA7 simulations. This is accompanied by a much smaller rainfall
328 overestimation in the tropical Indian Ocean in GA7 compared with GA6. Such results
329 are consistent with the findings from Bush et al. (2015) and Willetts et al. (2017), which
330 suggested that excessive rain over the equatorial Indian Ocean warm waters might have
331 contributed to the lack of Indian monsoon rainfall. Our analysis further shows that this
332 may be particularly true in strong monsoon years (Fig. 2h). Similarly, the opposite
333 situation occurred over East Asia and the nearby Philippines Sea. The rainfall over the
334 nearby Philippian Sea and East Asia are worse overestimated and underestimated in
335 GA7 than that in GA6 particularly during the years of strong ISMR (Fig. 2h). Thus,
336 poor rainfall simulation in GA7 over East Asian monsoon region is also a concern for
337 model improvement.

338 Overall, the rainfall pattern correlations between GA7 (GA6) and observation
339 during years of strong and weak ISMR are 0.875 (0.811) and 0.800 (0.748) over the
340 lower latitude of Australian–Asian domain (30°S–40°N, 30°–180°E). Thus, the rainfall
341 simulation is improved in GA7 compared with GA6. Furthermore, the differences
342 between GA7 and GA6 over the Indian monsoon domain in years of strong ISMR are
343 much more significant than in years of weak ISMR (Figs. 2g, h). These improved
344 rainfall simulations in GA7 during strong ISMR years may help to better understand
345 the link between the improved ISMR and the more realistically simulated rainfall
346 teleconnections in GA7.

347 **4. Circulation anomalies**

348 Circulation anomalies associated with the ISMR are analyzed using regression and
349 partial regression of stream function and wind anomalies at 500 hPa onto the ISMRI
350 (Figure. 3). As shown in Fig. 3, two distinct barotropical wave trains originated from
351 the ISM region propagating northward and southward into the NH and SH subtropics
352 are observed in observations. In the NH, the full regressed circulation pattern resembles
353 the circumglobal teleconnection (Ding and Wang 2005). The magnitude of the
354 circumglobal teleconnection decreases sharply and only three centers are observed over
355 Eurasia after removing the signals of ENSO and IOD (Fig. 3d). In the SH, the
356 atmospheric responses also become weaker after removing the signals (Fig. 3d)
357 suggesting the dependent influences of ENSO, IOD and ISMR on the circulation.

358 Originated from the ISM region, the wave train first propagates westward to the
359 Arabian Peninsula creating a region of abnormally cyclonic circulation, then
360 northeastward to Central Asia, creating a region of abnormally anti-cyclonic circulation,
361 and then eastward to Mongolia and northern China, creating a region of abnormally
362 cyclonic circulation, and finally eastward to the northeast China and Korean Peninsula,
363 creating a region of abnormally anti-cyclonic circulation (Fig.3d). In the SH, the wave
364 train first propagates southwestward to tropical western Indian Ocean creating a region
365 of abnormally anti-cyclonic circulation, then southward across Indian Ocean creating a
366 region of abnormally cyclonic circulation over the subtropical Indian Ocean and anti-
367 cyclonic circulation over mid-latitude Indian Ocean and southwestern Australia (Fig.
368 3d). This is consistent with the investigation by Zhao et al. (2019), who noted that an

369 equivalent barotropic wave train originating from the Maritime Continent propagates
370 southward to subtropical Australia. The two tropical cyclonic circulations over Arabian
371 Peninsula and tropical western Indian Ocean excited by ISMR resemble the opposite
372 signs of Gill-type responses to tropical diabatic heating (Gill 1980) as discussed in Jin
373 et al. (2019, cf. their Fig. 10). The atmospheric response patterns over Australia-Asia
374 monsoon region are observed in GA7, whereas the anomalous anti-cyclonic
375 circulations over Central Asia and subtropical Indian Ocean are not captured by GA6.
376 Furthermore, the abnormally cyclonic circulation over midlatitude Indian Ocean is
377 underestimated in GA6.

378 Figure 4 shows a map of partial regression of vertical velocity and geopotential
379 height anomalies at 500 hPa onto the ISMRI removing the signals of ENSO and IOD.
380 In the regions downstream of the troughs (cyclones) ascending anomalies are observed,
381 while in the regions downstream of the ridges (anti-cyclones) subsidence anomalies are
382 observed (Fig. 4). This vertical motions correspond to the westward tilt structure of the
383 extratropical atmosphere. The anomalous vertical velocity pattern associated with the
384 ISMR bears a strong resemblance to the rainfall pattern shown in Fig. 1. In particular,
385 the anomalous subsidence motions over Central Asia and Japanese islands which are
386 not conducive to the formation of precipitation are better simulated in GA7 than that in
387 GA6 (Figs. 4b, c). The subsidence anomaly over equatorial Indian Ocean and ascending
388 anomaly over central Australia are overestimated in GA6 but significantly improved in
389 GA7 (Figs. 4b, c). In addition, the vertical motion is opposite in the south and north
390 ISM region, which is not well simulated in both GA6 and GA7 (Figs. 4b, c).

391 Moisture transport at 850 hPa is also examined to gain further insight into the
392 moisture source associated with the ISMR. Figure 5 shows the partial correlation
393 between moist flux transports at 850 hPa and ISMR in observation and GA7, GA6
394 excluding the effects of ENSO and IOD. The anomalous moisture transports are close
395 to the circulation anomalies in Figure 3 indicating the important role of advection in the
396 moisture transports associated with the ISMR. As shown in Figure 5, the northward
397 anomalous moisture flux transports over East Asia and anti-cyclonic moisture flux
398 transports over subtropical Indian Ocean are better simulated in GA7 contributing to
399 the precipitation increase over northern China and southwest Australia respectively.
400 Particularly, the moisture transports are underestimated over subtropical Indian Ocean
401 and overestimated over central Australia in GA6 which is corresponded to the rainfall
402 anomalies (Fig. 5c). Overall, the influences of ISMR-teleconnection on the vertical
403 motions and moisture transports lead to the formation of rainfall teleconnection.
404 Therefore, the better simulated ISMR-teleconnection helps to improve the presentation
405 of extratropical rainfall in the models.

406 **5. Rossby wave ray tracing and the role of the meridional basic flow**

407 Rossby wave ray tracing in a horizontally non-uniform flow, which describes the
408 pathways of Rossby wave dispersion, is adopted to investigate the link between the
409 improved ISMR and the associated rainfall teleconnections. Technical details about the
410 wave ray tracing analysis can be found in Zhao et al. (2015, 2019). Before describing
411 the wave ray, the background flow is analyzed. Figure 6 shows the composite difference

412 in full regressed and partial regressed wind anomalies at 250 hPa between strong and
413 weak ISMR years. The partial regressed anomalous winds are similar to that full
414 regressed, but with slight changes in the magnitude of wind anomalies in GA7 and
415 observation suggesting the independent influences of ENSO, IOD and ISMR on the
416 upper tropospheric wind in observation and GA7. As shown in Fig6., the anti-cyclonic
417 circulations over Central Asia and East Asia and a cyclonic circulation over subtropical
418 Indian Ocean (Fig. 6) are in good agreement with the results of Wang et al. (2001, cf.
419 their Fig. 8). Particularly, this anomalous circulation pattern is close to the circulation
420 pattern at 500 hPa associated with the ISMR (Figs. 3e, f) indicating that the response
421 of the extratropical atmosphere to the ISMR is quasi-barotropic. The background flow
422 used to calculate the stationary wave ray trajectories is the superposition of the
423 composite of partial regressed anomalous wind and the climatology wind.

424 **5.1 Rossby wave ray tracing**

425 Figure 7 illustrates the stationary wave ray trajectories of zonal wavenumbers 2–5
426 emanating from ISMR sources in observations, GA7, and GA6. The wave rays first
427 propagate westward to tropical Africa, then divide to propagate to the NH and SH
428 subtropics (Fig. 7). Evidently, the southern branch of the wave rays in years of strong
429 ISMR is more evident than that in years of weak ISMR, indicating the likely diabatic
430 heating influence of ISMR on the cross equatorial Rossby wave propagation.
431 Furthermore, the wave rays in the SH subtropics are much more than those in the NH
432 in observations (Figs. 7a, b, c), leading to stronger wave trains in the SH (Figs. 3a, b).

433 This is better captured by GA7 during years of strong ISMR (Fig. 7e) than GA6 (Fig.
434 7h). On the other hand, both GA6 and GA7 simulate weaker wave propagation in the
435 SH than that observed in years of weak ISMR (Figs. 7f, i), although in GA7, the
436 propagation towards tropical Africa is somewhat closer to observations (Fig. 7f).

437 The situation is similar for the northern branch of wave rays. The northern wave-
438 ray characteristics simulated in GA7 in years of strong ISMR are much closer to
439 observations than in GA6, with wave rays occurring in the subtropical westerlies over
440 Asia (Figs. 7b, e). However, during years of weak ISMR, the northern branch of the
441 wave rays in both GA7 and GA6 are poorly simulated (Figs. 7f, i), with wave rays
442 being much stronger and further poleward than in observations. Both GA6 and GA7
443 perform poorly in reproducing the observed characteristics of wave rays in weak ISMR
444 years, during which both model configurations showed a significant dry bias over the
445 Indian monsoon domain in JJA (Fig. 2). Nevertheless, it is not clear whether we can
446 directly associate the poor simulation of wave rays with the underestimation of ISMR.
447 This is because during weak ISMR years, one would expect weak diabatic heating over
448 the Indian monsoon region. However, without considering the diabatic influence of
449 deep monsoon convection on the mean flow, the increase of isolated equatorially
450 asymmetric heating only strengthens the atmospheric response, but not vary the
451 atmospheric patterns (Xing et al., 2014). We need to investigate further to what extent
452 the model's failure to reproduce wave propagation in weak monsoon years is because
453 of the poor simulation of the atmospheric mean flow in the region, or because of the
454 significant lack of rainfall during those years.

455 **5.2 Meridional wind ducts in the upper troposphere**

456 According to the studies by Zhao et al. (2015, 2019) and Li et al. (2015), the
457 meridional basic flow plays an important role in facilitating the propagation of
458 stationary Rossby wave. Furthermore, the interhemispheric propagation of Rossby
459 waves is dominated largely by the meridional flow (Lee et al., 2013; Liu and Wang,
460 2013; Li et al., 2015; Zhao et al., 2015, 2019). Figure 7 shows the 250 hPa horizontal
461 winds from ERA-interim, GA7, and GA6 in JJA. As shown in Fig. 7a, strong easterly
462 winds prevail at upper levels over the tropical Australian–Asian and African monsoon
463 regions. In tropical North Africa, southerly winds prevail between 10°N and 30°N,
464 whilst northerly winds prevail below 10°N, causing the Rossby wave to first propagate
465 westward and then divide northward and southward over tropical North Africa and
466 beyond. Similarly, the northerly winds over the Indian subcontinent and tropical Indian
467 Ocean also lead the Rossby wave to propagate southward into the SH. The southerly
468 winds prevailing over the western Tibetan Plateau drive the Rossby wave northward
469 into the Asian subtropical westerlies.

470 The poor simulated meridional propagation of Rossby wave is closely related to the
471 modelling errors of the meridional wind. The significantly weak simulated northerly
472 winds over the upper tropospheric South Asian monsoon domain in GA6 (Figs. 8e, f)
473 are not favorable to the cross-equatorial propagation of Rossby wave. Furthermore, the
474 strength of the simulated meridional winds in Asia in GA6 are stronger than that shown
475 in observations (Figs. 8e, f), especially for the southerly winds over the western Tibetan
476 Plateau. This contributes to the stronger and further poleward propagation of Rossby

477 wave in GA6 (Figs. 7g, h, i). In contrast, the upper tropospheric meridional winds over
478 the western Tibetan Plateau and south Asian monsoon are more realistically simulated
479 in GA7 (Fig. 8d), especially in years of strong ISMR (Fig. 8h). Therefore, analyzing to
480 what extent the simulation of ISMR influence the meridional wind will help to
481 understand the contribution of improvement of ISMR to the Rossby wave propagation.
482 Furthermore, as discussed by Jin et al. (2019) the SAH is closely linked to the diabatic
483 heating effect of the tropical Indian monsoon, the influence of SAH on the meridional
484 wind will also be considered.

485 The strength of SAH is defined as the averaged geopotential height of grid within
486 the isoline of 12500 gpm at 200 hPa (Figures 9g, h, i). The multiple regression is used
487 to measure the linear contributions of ISMR and SAH to the meridional wind.
488 Considering the relationship between SAH and ISMR, we removed the linear effect of
489 SAH on ISMR through partial regression. Fig. 9 shows the climatology of SAH and the
490 multiple regression of meridional wind on the ISMRI and SAHI. As shown in Fig. 9,
491 the meridional winds over South Asian monsoon region in GA6 and GA7 is closely
492 related to ISMR. With the increase of ISMR, stronger convective activity enhances the
493 Indian monsoon circulation, the upper northerly wind over South Asian monsoon region
494 enhances (Fig. 8h), making stronger cross equatorial Rossby wave (Fig. 7e).
495 Furthermore, the relationship between anomalous northerly wind over western Tibetan
496 Plateau and ISMR is better simulated in GA7 than that in GA6 (Figs. 9b, c). Moreover,
497 the contribution of SAH to the upper meridional wind over South Asian monsoon
498 region in GA7 are better simulated than that in GA6 (Figs. 9e, f). Therefore, both the

499 enhancement of ISMR and SAH during years of strong ISMR in GA7 contribute to the
500 more realistic meridional wind over south Asian monsoon and western Tibetan Plateau,
501 and hence make more realistic propagation of Rossby wave.

502 What's more, the simulation of SAH in GA7 is improved significantly compared
503 with that in GA6. Due to the dynamic relationship between wind and pressure, the
504 simulation of wind improves with the improvement of pressure. Particularly, at
505 midlatitudes, the pressure dominates the wind according to the geostrophic relationship.
506 As a result, the improvement of SAH in GA7 leads to more realistic climatic mean flow
507 over South Asia than that in GA6 (Figs. 9g, h, i). In particular, the much stronger
508 southerly wind over western Tibetan Plateau and south Asian monsoon region in GA6
509 is mainly owing to the poor simulation of SAH (Fig. 9i). Furthermore, the
510 improvement of ISMR intensity with more realistic convective heating in GA7
511 contributes to more realistic meridional wind over South Asian monsoon region.

512 Nevertheless, it still has to point out that the inter-annual variability of ISMR in
513 GA7 needs to be improved, and the relationship between SAH and ISMR is
514 overestimated in GA6 and GA7 with the correlation coefficients of 0.48 and 0.33,
515 respectively, while 0.13 in the observation. The significant improvement of SAH in
516 GA7 corresponds to the skillfully simulated ISMR, which may own to the deeper
517 convection and more realistic diabatic heating are allowed in GA7 (Walters et al. 2019).

518 **6. Summary and discussion**

519 In this study, we have investigated the link between the improved simulation of
520 ISMR and the associated extratropical rainfall teleconnections in two versions of the

521 UKMO Unified Model, GA6 and GA7, using Rossby wave ray tracing theory (Li and
522 Li et al., 2012; Li et al., 2015; Zhao et al., 2015, 2019). In a previous UM assessment
523 study, Jin et al. (2019) reported that the reduced Indian monsoon dry bias in UM GA7
524 at N216 resolution led to more realistic monsoon rainfall teleconnection patterns.
525 However, they did not conduct detailed wave propagation analysis to support these
526 results. Therefore, our study focused on investigating Rossby wave propagation in these
527 two model configurations by using Rossby wave ray tracing in a horizontally
528 nonuniform background flow, as in Zhao et al. (2015, 2019).

529 Our observational analysis showed that the diabatic heating associated with ISMR
530 can excite two distinct wave trains in the NH and SH subtropics. GA7 can better
531 simulate the teleconnections associated with the ISMR over Australia-Asia monsoon
532 region compared with GA6. The realistic simulated atmospheric teleconnection in GA7
533 plays an important role in the improvement of rainfall teleconnection by modulating
534 the vertical motion and the moisture transport.

535 The teleconnection wave train coincides with the pathway of the stationary
536 Rossby wave propagation. Driven by the upper tropospheric easterly flow, the
537 stationary Rossby wave first propagate westward, then separate into northern and
538 southern branches following the meridional wind ducts. The northern branch mainly
539 propagates in the subtropical westerlies over Asia and the southern branch primarily
540 propagates in the SH subtropical westerlies. Compared with GA6, GA7 can better
541 capture the characteristics of Rossby wave propagation pathways in years of strong
542 ISMR, with stronger cross-equatorial propagation and a more realistic northern branch

543 of the wave ray tracing trajectories. This was attributed largely to the model skillfully
544 simulating of ISMR and SAH, and their influences on the meridional basic flow over
545 upper South Asia monsoon and western Tibetan Plateau.

546 Our study may also provide new insights for monsoon teleconnection evaluations
547 by revealing the Rossby wave propagation pathway from the upper tropospheric
548 easterlies. The upper tropospheric meridional winds associated with the monsoon
549 system play an important role in Rossby wave propagation and hence improve the
550 simulation of tropical monsoon teleconnections. Sakaguchi et al. (2016) detected
551 changes in Rossby wave ray trajectories influenced by Asian monsoon rainfall and the
552 associated basic flow using different grid refinements in the Community Atmosphere
553 Model version 4. The teleconnection pathways revealed by Rossby wave ray
554 trajectories provide implications for evaluating and improving the model's performance
555 of simulating tropical monsoon teleconnections.

556 The analysis in this paper was focused mainly on the Australian–Asian monsoon
557 region, but further research could be done to evaluate the influence of the tropical Asian
558 monsoon on the weather and climate over other regions. It is also worth noting that
559 significant deficiencies in the modelling of ISMR remain, despite the reduced dry bias
560 in GA7. In particular, the northerly wind ducts over the upper tropospheric South Asian
561 monsoon region in GA7 are poorly simulated. Walter et al. (2019) indicated that the
562 southern branch of the Hadley circulation during JJA in GA7 using an N216 grid was
563 improved significantly compared with GA6 at the same resolution, due to the deeper
564 convection in GA7. Thus, the simulation of convection is important to improve the

565 simulation of circulation and tropical monsoon teleconnections.

566 We acknowledge that the datasets used in the current analysis come from the
567 atmosphere-only configuration of the UM. It is important to conduct a similar analysis
568 with globally coupled simulations (Williams et al., 2017) to better understand the
569 rainfall teleconnections that could be modulated by air–sea interactions. This will also
570 help us to assess whether current model deficiencies in simulating the Australian–Asian
571 monsoon system can affect the climate and climate change outside the monsoon domain
572 simulated by current CMIP models.

573

574 **Acknowledgements**

575 This work was jointly supported by the National Natural Science Foundation of China (NSFC,
576 41530424 and 41790474) projects, Shandong Natural Science Foundation Project
577 (ZR2019ZD12) and Fundamental Research Funds for the Central Universities (201962009).
578 HZ acknowledges the UM partnership for making the model simulations available and
579 supporting this study. HZ and JL appreciate the discussions with scientists at the UM Global
580 Teleconnection Workshop, Met Office, UK 17-26 June 2019.

581

582 **References**

- 583 Adler RF et al (2003) The version 2 Global Precipitation Climatology Project (GPCP)
584 monthly precipitation analysis (1979–present). *J Hydrometeorol* 4:1147–1167
- 585 Anand A, Mishra, SK, Sahany S, Bhowmick M, Rawat JS, Dash SK (2018) Indian
586 summer monsoon simulations: usefulness of increasing horizontal resolution,
587 manual tuning, and semi-automatic tuning in reducing present-day model
588 biases. *Sci Reports* 8(1):3522
- 589 Anderson TW (1984) *An Introduction to Multivariate Statistical Analysis*, 2nd edn.
590 Wiley, New York, pp 675
- 591 Ashok K, Guan Z, Yamagata T (2001) Impact of the Indian Ocean Dipole on the
592 relationship between the Indian monsoon rainfall and ENSO. *Geophys Res Lett*
593 28:4499–4502
- 594 Branstator G (1983) Horizontal energy propagation in a barotropic atmosphere with
595 meridional and zonal structure. *J Atmos Sci* 40:1689–1708
- 596 Branstator G (1985) Analysis of general circulation model sea-surface temperature
597 anomaly simulations using a linear model. Part I: Forced solutions. *J Atmos Sci*
598 42:2225–2241
- 599 Bush SJ, Turner AG, Woolnough SJ, Martin GM, Klingaman NP (2015) The effect of
600 increased convective entrainment on Asian monsoon biases in the MetUM general
601 circulation model. *Q J R Meteorol Soc* 141:311–326.
- 602 Ding Q, Wang B (2005) Circumglobal teleconnection in the Northern Hemisphere
603 summer. *J. Clim* 18:3483–3505
- 604 Ding Q, Wang B (2007) Intraseasonal teleconnection between the summer Eurasian
605 wave train and the Indian monsoon. *J Clim* 20:3751–3767
- 606 Ding Q, Wang B, Wallace JM, Branstator G (2011) Tropical–extratropical
607 teleconnections in boreal summer: Observed interannual variability. *J Clim*
608 24:1878–1896. <http://doi.org/10.1175/2011JCLI3621.1>
- 609 Dee DP et al (2011) The ERA-Interim reanalysis: configuration and performance of the
610 data assimilation system. *Q J R Meteorol Soc* 137:553–597

611 Enomoto T, Hoskins BJ, Matsuda Y (2003) The formation mechanism of the Bonin
612 high in August. Q J R Meteorol Soc 129:157–178.
613 <http://doi.org/10.1256/qj.01.211>

614 Gill AE (1980) Some simple solutions for heat-induced tropical circulation. Q J R
615 Meteorol Soc 106(449):447–462. <https://doi.org/10.1002/qj.49710644905>

616 Gregory D, Rowntree PR (1990) A Mass Flux Convection Scheme with Representation
617 of Cloud Ensemble Characteristics and Stability-Dependent Closure. Monthly
618 Weather Review 118(7):1483–1506. [https://doi.org/10.1175/1520-
619 0493\(1990\)118<1483:AMFCSW>2.0.CO;2](https://doi.org/10.1175/1520-0493(1990)118<1483:AMFCSW>2.0.CO;2)

620 Gregory D, Allen S (1991) The effect of convective scale downdraughts upon NWP
621 and climate simulations. In: 9th conference on numerical weather prediction.
622 Amer Meteorol Soc 122–123

623 Hirst A (2015) Towards CMIP6: plans for participation by ACCESS. In: CAWCR 9th
624 annual workshop 19–22

625 Hoskins BJ, Rodwell MJ (1995) A model of the Asian summer monsoon. Part I: the
626 global scale. J Atmos Sci 52:1329–1340

627 Hoskins BJ, Karoly DJ (1981) The steady linear response of a spherical atmosphere to
628 thermal and orographic forcing. J Atmos Sci 38(6):1179–1196.
629 [https://doi.org/10.1175/1520-0469\(1981\)038<1179:TSLROA>2.0.CO;2](https://doi.org/10.1175/1520-0469(1981)038<1179:TSLROA>2.0.CO;2)

630 Hudson D et al (2017) ACCESS-S1: the new Bureau of Meteorology multi-week to
631 seasonal prediction system. J South Hemisph Earth Syst Sci 67:132–159

632 Karoly DJ (1989) Southern Hemisphere Circulation Features Associated with El Niño-
633 Southern Oscillation Events. J Clim 2(11):1239–1252

634 Kim B-J, Moon S-E, Lu R, Kripalani RH (2002) Teleconnections: summer monsoon
635 over Korea and India. Adv Atmos Sci 19:665–676

636 Kripalani RH, Kulkarni A, Singh SV (1997) Association of the Indian summer
637 monsoon with the Northern Hemisphere mid-latitude circulation. Int J Climatol
638 17:1055–1067

639 Lau K-M, Lim H (1984) On the dynamics of equatorial forcing of climate
640 teleconnections. J Atmos Sci 41:161–176

641 Lee SK, Mechoso CR, Wang C, Neelin JD (2013) Interhemispheric influence of the
642 northern summer monsoon on southern subtropical anticyclones. *J Clim*
643 26(24):10193–10204

644 Lee SK, Wang C, Mapes BE (2009) A simple atmospheric model of the local and
645 teleconnection responses to tropical heating anomalies. *J Clim* 22(2):272–284.
646 <https://doi.org/10.1175/2008jcli2303.1>

647 Li L, Nathan TR (1994) The global atmospheric response to low-frequency tropical
648 forcing: Zonally averaged basic states. *J Atmos Sci* 51:3412–3426

649 Li JP, Zeng QC (2002) A unified monsoon index. *Geophys Res Lett* 29(8):115-1-115-
650 4

651 Li JP, Zeng QC (2003) A new monsoon index and the geographical distribution of the
652 global monsoons. *Adv Atmos Sci* 20:299–02

653 Li JP, Zeng QC (2005) A new monsoon index, its interannual variability and relation
654 with monsoon precipitation. *Climatic Environ Res (in Chinese)* 10(3):351-365

655 Li JP, Wu GX, Hu DX et al (2011) *Ocean-Atmosphere Interaction over the Joining
656 Area of Asia and Indian-Pacific Ocean and Its Impact on the Short-Term Climate
657 Variation in China (Volume I)*. Beijing: China Meteorol Press 1–30

658 Li JP et al (2013) Progress in air–land–sea interactions in Asia and their role in global
659 and Asian climate change (in Chinese). *Chin J Atmos Sci* 37:518–538

660 Li JP, Ruan CQ (2018) The North Atlantic–Eurasian teleconnection in summer and its
661 effects on Eurasian climates. *Environ Res Lett* 13:024007.
662 <https://doi.org/10.1088/1748-9326/aa9d33>

663 Li JP, Zheng F, Sun C, Feng J, Wang J (2019) Pathways of influence of the Northern
664 Hemisphere mid–high latitudes on East Asian climate: A Review. *Adv Atmos Sci*
665 36:902–921

666 Li Y, Li JP (2012) Propagation of planetary waves in the horizontal non-uniform basic
667 flow (in Chinese). *Chin J Geophys* 55(2):361–371.
668 <https://doi.org/10.6038/j/issn.0001-5733.2012.02.001>

669 Li Y, Li JP, Feng J (2013) Boreal summer convection oscillation over the Indo-Western
670 Pacific and its relationship with the East Asian summer monsoon. *Atmos Sci Lett*

671 14(2):66–71

672 Li Y, Li JP, Jin FF, Zhao S (2015) Interhemispheric propagation of stationary Rossby
673 waves in the horizontally nonuniform background flow. *J Atmos Sci* 72(8):3233–
674 3256. <https://doi.org/10.1175/JAS-D-14-0239.1>

675 Lighthill J (1978) *Waves in Fluids*. Cambridge University Press, pp 540

676 Lin, H (2009) Global extratropical response to diabatic heating variability of the Asian
677 summer monsoon. *J Atmos Sci* 66:2697–2713

678 Liu F, Wang B (2013) Mechanisms of global teleconnections associated with the Asian
679 summer monsoon: An intermediate model analysis. *J Clim* 26:1791–1806.
680 <http://doi.org/10.1175/JCLI-D-12-00243.1>

681 Lu R, Oh J-H, Kim B-J (2002) A teleconnection pattern in upper-level meridional wind
682 over the North African and Eurasian continent in summer. *Tellus* 54A:44–55,
683 <http://doi.org/10.3402/tellusa.v54i1.12122>

684 Jiang X, Li Y, Yang S, Wu R (2011) Interannual and interdecadal variations of the
685 South Asian and western Pacific subtropical highs and their relationships with
686 Asian-Pacific summer climate. *Meteorol Atmos Phys* 113:171–180

687 Jin L, Zhang H, Moise A, Martin G, Milton S, Rodriguez J (2019) Australia-Asian
688 monsoon in two versions of the UK Met Office Unified Model and their impacts
689 on tropical–extratropical teleconnections. *Clim Dyn* 53(7–8):4717–4741

690 MacLachlan C et al (2015) Description of GloSea5: the Met Office high resolution
691 seasonal forecast system. *Q J R Meteorol Soc* 1:1. <https://doi.org/10.1002/qj.2396>

692 Martin GM, Milton SF, Senior CA, Brooks ME, Ineson S (2010) Analysis and reduction
693 of systematic errors through a seamless approach to modeling weather and climate.
694 *J Clim* 23:5933–5957

695 Nitta T (1987) Convective activities in the tropical western Pacific and their impacts
696 on the Northern Hemisphere summer circulation. *J Meteorol Soc Japan* 65:373–
697 390

698 Nitta T (1989) Global features of the Pacific–Japan oscillation. *Meteorol Atmos Phys*
699 41:5–12. <http://doi.org/10.1007/BF01032585>

700 Ning L, Liu J, Wang B (2017) How does the South Asian High influence extreme

701 precipitation over eastern China? *J Geophys Res Atmos* 122:4281–4298

702 Prakash S, Mitra AK, Momin IM, Rajagopal EN, Milton SF, Martin GM (2016) Skill
703 of short to medium range monsoon rainfall forecasts from two global models over
704 India for hydrometeorological applications. *Meteorol Appl* 23:574–586

705 Puri K et al (2013) Implementation of the initial ACCESS numerical weather prediction
706 system. *Aust Meteorol Ocean* 63:265–284

707 Ringer MA et al (2006) The physical properties of the atmosphere in the new Hadley
708 Centre global environmental model (HadGEM1). Part II: aspects of variability
709 and regional climate. *J Clim* 19:1302–1326

710 Saji NH, Goswami BN, Vinayachandran PN, Yamagata T (1999) A dipole mode in the
711 tropical Indian Ocean. *Nature* 40:360–363

712 Sakaguchi K, Lu J, Leung LR, Zhao C, Li Y, & Hagos S (2016) Sources and pathways
713 of the upscale effects on the Southern Hemisphere jet in MPAS-CAM4 variable-
714 resolution simulations. *J Adv Model Earth Syst* 8(4): 1786 – 1805.
715 <https://doi.org/10.1002/2016MS000743>

716 Sardeshmukh P, Hoskins B (1988) The generation of global rotational flow by steady
717 idealized tropical divergence. *J Atmos Sci* 45:1228–1251

718 Schneider EK, Watterson IG (1984) Stationary Rossby wave propagation through
719 easterly layers. *J Atmos Sci* 41:2069–2083

720 Shaman J, Samelson RM, Tziperman E (2012) Complex wavenumber Rossby wave ray
721 tracing. *J Atmos Sci* 69:2112–2133

722 Simmons A J (1982) The forcing of stationary wave motion by tropical diabatic heating.
723 *Q J R Meteorol Soc* 108:503–534

724 Sperber KR, Annamalai H, Kang IS, Kitoh A, Moise A, Turner A, Wang B, Zhou T
725 (2013) The Asian summer monsoon: an intercomparison of CMIP5 vs. CMIP3
726 simulations of the late 20th century. *Clim Dyn* 41:2711–2744

727 Walters D et al (2014) The Met Office unified model global atmosphere 4.0 and JULES
728 global land 4.0 configurations. *Geosci Model Dev* 7:361–386

729 Walters D et al (2017) The Met Office unified model global atmosphere 6.0/6.1 and

730 JULES global land 6.0/6.1 configurations. *Geosci Model Dev* 10:1487–1520
731 Walters D et al (2019) The Met Office unified model global atmosphere 7.0/7.1 and
732 JULES global land 7.0 configurations. *Geosci Model Dev* 12:1909–1963
733 Wang B, Wu R, Lau K-M (2001) Interannual variability of the Asian summer monsoon:
734 Contrasts between the Indian and the western North Pacific–East Asian monsoons.
735 *J. Clim* 14:4073–4090
736 Wei W, Zhang R, Wen M, Rong X, Li T (2014) Impact of Indian summer monsoon on
737 the South Asian High and its influence on summer rainfall over China. *Clim Dyn*
738 43:1257–1269
739 Wei W, Zhang R, Wen M, Kim B-J, Nam J-C (2015) Interannual variation of the South
740 Asian High and its relation with Indian and East Asian summer monsoon rainfall.
741 *J Clim* 28:2623–2634
742 Whitham G (1960) A note on group velocity. *J Fluid Mech* 9:347–352.
743 <http://doi.org/10.1017/S0022112060001158>
744 Willetts PD, Marsham JH, Birch CE, Parker DJ, Webster S, Petch J (2017) Moist
745 convection and its upscale effects in simulations of the Indian monsoon with
746 explicit and parametrized convection. *Q J R Meteorol Soc* 143(703):1073–1085
747 Williams KD et al (2017) The Met Office Global Coupled model 3.0 and 3.1 (GC3.0
748 and GC3.1) configurations. *J Adv Model Earth Syst* 10:357–380
749 Wilson DR, Ballard SP (1999) A microphysically based precipitation scheme for the
750 UK meteorological office unified model. *Q J R Meteorol Soc* 125(557):1607–
751 1636. <http://doi.org/10.1002/qj.49712555707>
752 Wood N et al (2014) An inherently mass-conserving semi-implicit semi-Lagrangian
753 discretization of the deep-atmosphere global non-hydrostatic equations. *Q J R*
754 *Meteorol Soc* 140:1505–1520
755 Wu R (2002) A mid-latitude Asian circulation anomaly pattern in boreal summer and
756 its connection with the Indian and East Asian summer monsoons. *Int J Climatol*
757 22:1879–1895
758 Wu R (2017) Relationship between Indian and east Asian summer rainfall variations.
759 *Adv Atmos Sci* 34:4–15

760 Xing N, Li JP, Li Y (2014) Response of the tropical atmosphere to isolated equatorially
761 asymmetric heating. *Chin J Atmos Sci* 38(6):1147–1158.
762 <https://doi.org/10.3878/j.issn.1006-9895>

763 Zhang H, McGuffie K, Henderson-Sellers A (1996) Impacts of tropical deforestation
764 II: the role of large-scale dynamics. *J. Climate* 9:2498-2521

765 Zhang P, Liu Y, He B (2016) Impact of East Asian summer monsoon heating on the
766 interannual variation of the South Asian High. *J Clim* 29:159–173

767 Zhao Y, Huang AN, Zhou Y, Huang DQ (2014) Impact of the middle and upper
768 tropospheric cooling over central Asia on the summer rainfall in the Tarim Basin,
769 China. *J Clim* 27:4721–4732

770 Zhao S, Li JP, Li Y (2015) Dynamics of an interhemispheric teleconnection across the
771 critical latitude through a southerly duct during boreal winter. *J Clim* 28(19):7437–
772 7456. <https://doi.org/10.1175/JCLI-D-14-00425.1>

773 Zhao S, Li JP, Li Y, Jin F-F, Zheng J (2018) Interhemispheric influence of Indo-Pacific
774 convection oscillation on Southern Hemisphere rainfall through southward
775 propagation of Rossby waves. *Clim Dyn* 52(5-6):3203–3221

776 Zhao Y, Zhang HQ (2016) Impacts of SST warming in tropical Indian Ocean on CMIP5
777 model-projected summer rainfall changes over Central Asia. *Clim Dyn* 46:3223–
778 3238

779

780 **Figure captions**

781 Figure 1. Correlation map of JJA rainfall with ISMRI for the period 1982–2008 (a)
782 GPCP; (b) GA7; (c) GA6. (d)–(f) Same as (a)–(c), respectively, but for partial
783 correlation excluding the signals of both ENSO and IOD. Dotted areas denote
784 significance at the 95% confidence level. The ‘R’ at the top right of (b)–(c) indicates
785 the pattern correlation (30°–180°E, 50°S–60°N) with (a), and the ‘R’ at the top right of
786 (e)–(f) indicates the pattern correlation with (b) respectively. The black box denotes the
787 Indian summer monsoon domain (70°–90°E, 5°–25°N). The solid black lines represent
788 the pathways of the rainfall teleconnection.

789 Figure 2. Composites of strong/weak summer monsoon rainfall (JJA) for the period
790 1982–2008 (unit: mm day⁻¹). (a), (b) GPCP observations; (c), (d) GA6; (e), (f) GA7;
791 and (g), (h) difference between GA7 and GA6. The black box represents the Indian
792 summer monsoon domain. Cross hatched areas denote significance at the 90%
793 confidence level. Strong (weak) monsoon years are determined based on when the
794 ISMRI (normalized area-averaged summer rainfall anomalies over 70°–90°E, 5°–25°N)
795 is above (below) 0.75 (–0.75).

796 Figure 3. Map of regression of stream function (shading; units: m² s⁻¹) and anomalous
797 wind (vectors; units: m s⁻¹) at 500 hPa onto ISMRI (a) ERA-Interim; (c) GA7; (e) GA6.
798 (b), (d), (f) Same as (a), (c), (e), respectively, but for partial regression excluding the
799 signals of both ENSO and IOD. Dotted areas denote significance at the 95% confidence
800 level; only vectors significant at the 95% confidence level are shown.

801 Figure 4. Map of the partial regression of vertical velocity (shading; units: m s⁻¹) and
802 geopotential height anomalies (contour; units: m) at 500 hPa onto ISMRI excluding the
803 linear effects of ENSO and IOD (a) ERA-Interim; (b) GA7; (c) GA6. Cross hatched
804 areas denote significance at the 90% confidence level.

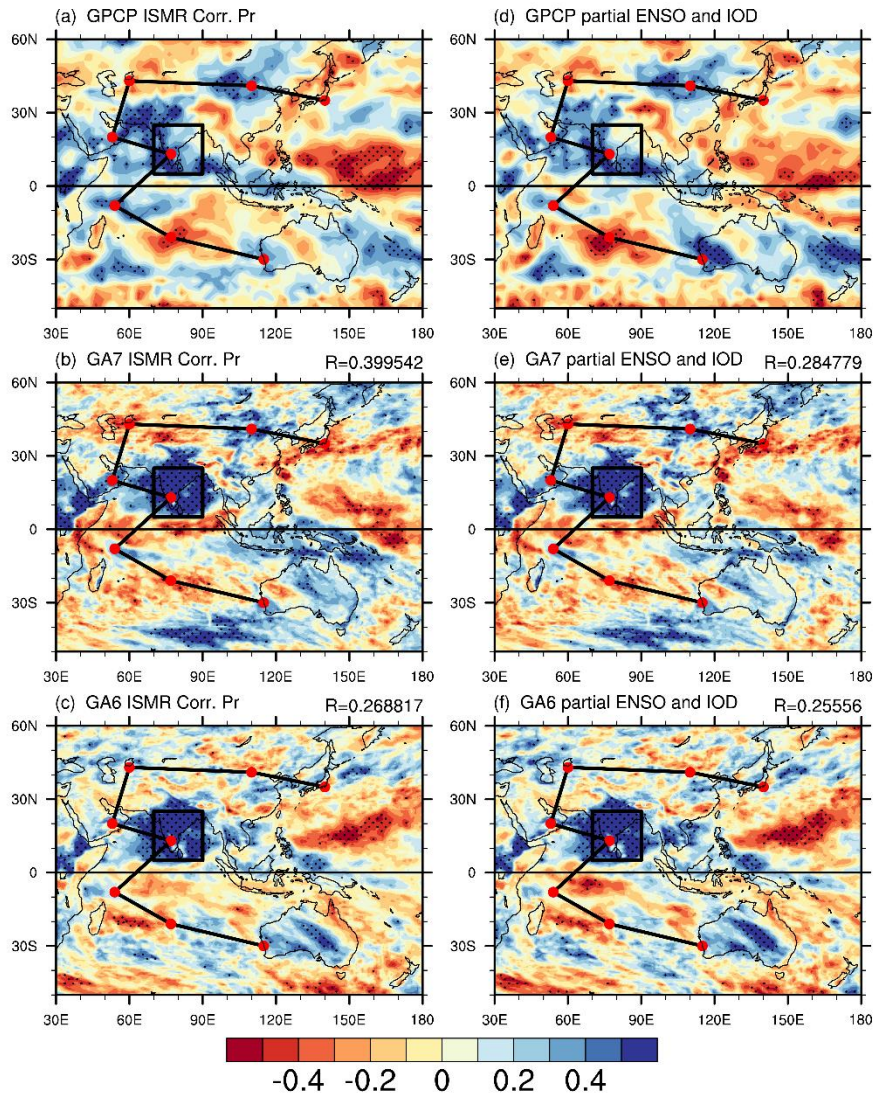
805 Figure 5. Partial correlation map of JJA rainfall (shading; units: mm) and moisture flux
806 at 850 hPa (vectors; units: mm) with ISMRI excluding the signals of ENSO and IOD
807 (a) GPCP; (b) GA7; (c) GA6. Only shading and vectors significant at the 90%
808 confidence level are shown.

809 Figure 6. Map of regression of anomalous horizontal wind (vectors; units: m s^{-1}) at 250
810 hPa onto ISMRI (a) ERA-Interim; (c) GA7; (e) GA6. (b), (d), (f) Same as (a), (c), (e),
811 respectively, but for partial regression excluding the linear influence of ENSO and IOD.
812 Shaded areas denote significance at the 90% confidence level.

813 Figure 7. Stationary Rossby wave ray trajectories (curves) initiated with zonal
814 wavenumbers 2–5 from ISMR sources (black dots), driven by the 250 hPa horizontal
815 wind, and excluding the influence of ENSO and the IOD. (a)–(c) ERA-Interim wind
816 data; (d)–(f) GA6; and (g)–(i) GA7. Red and green curves represent the stationary
817 Rossby waves propagating in the Southern and Northern Hemisphere, respectively.

818 Figure 8. 250 hPa climatological zonal winds (contours; unit: m s^{-1}) and meridional
819 winds (shading; unit: m s^{-1}) excluding the influence of ENSO and the IOD. (a) ERA-
820 Interim; (b) GA7; (c) GA6; (d) difference between GA7 and GA6. Difference between
821 GA6 and observations of composite meridional winds from years of (e) weak and (f)
822 strong ISMR. Difference between GA7 and GA6 of composite meridional winds from
823 years of (g) weak and (h) strong ISMR. Dotted areas represent significance at the 90%
824 confidence level.

825 Figure 9. Multiple regression of 200 hPa meridional wind to (a)–(c) ISMRI and (d)–(f)
826 SAHI. (g)–(f) Meridional geostrophic wind (shading; units: m s^{-1}) and geopotential
827 height (contour; units: m). The solid lines in (g)–(i) represent the location of the
828 climatological SAH, and the yellow and purple thick solid lines in (d)–(f) indicate the
829 composites location of SAH in the years of strong and weak ISMR. Top column is for
830 ERA-Interim, middle column is for GA7, and bottom column is for GA6.



832

833 Fig. 1. Correlation map of JJA rainfall with ISMRI for the period 1982–2008 (a) GPCP;

834 (b) GA7; (c) GA6. (d)–(f) Same as (a)–(c), respectively, but for partial correlation

835 excluding the signals of both ENSO and IOD. Dotted areas denote significance at the

836 95% confidence level. The ‘R’ at the top right of (b)–(c) indicates the pattern correlation

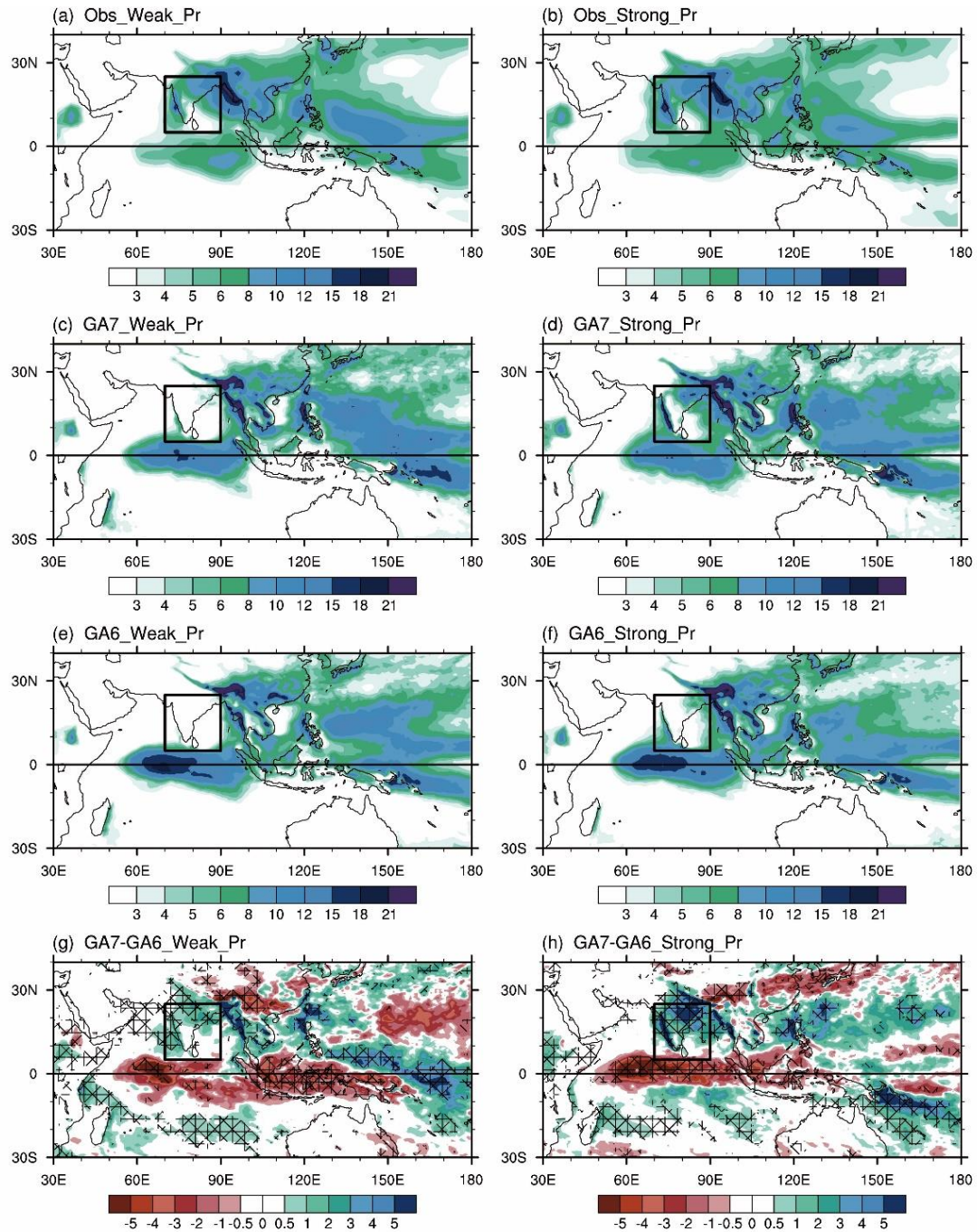
837 (30°–180°E, 50°S–60°N) with (a), and the ‘R’ at the top right of (e)–(f) indicates the

838 pattern correlation with (b) respectively. The black box denotes the Indian summer

839 monsoon domain (70°–90°E, 5°–25°N). The solid black lines represent the pathways

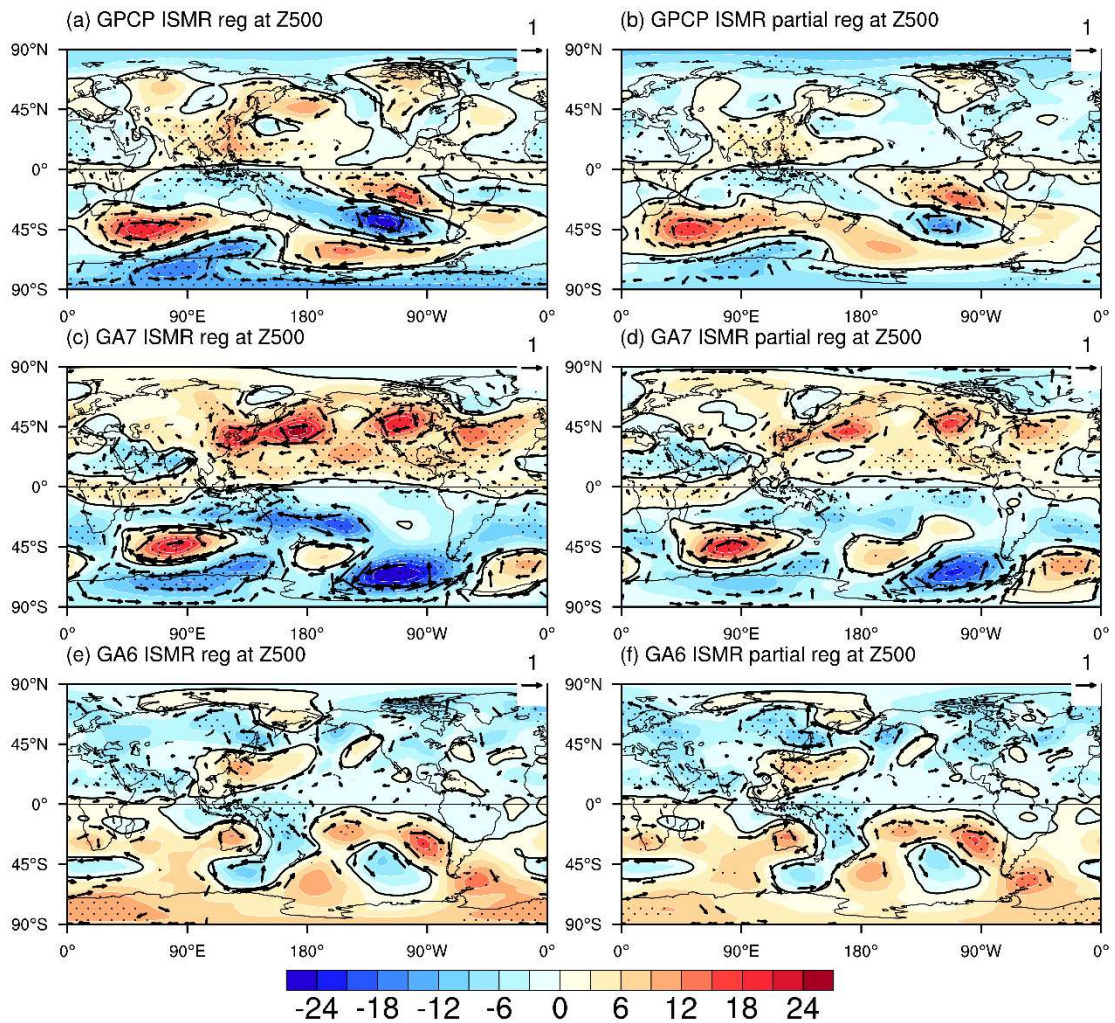
840 of the rainfall teleconnection.

841



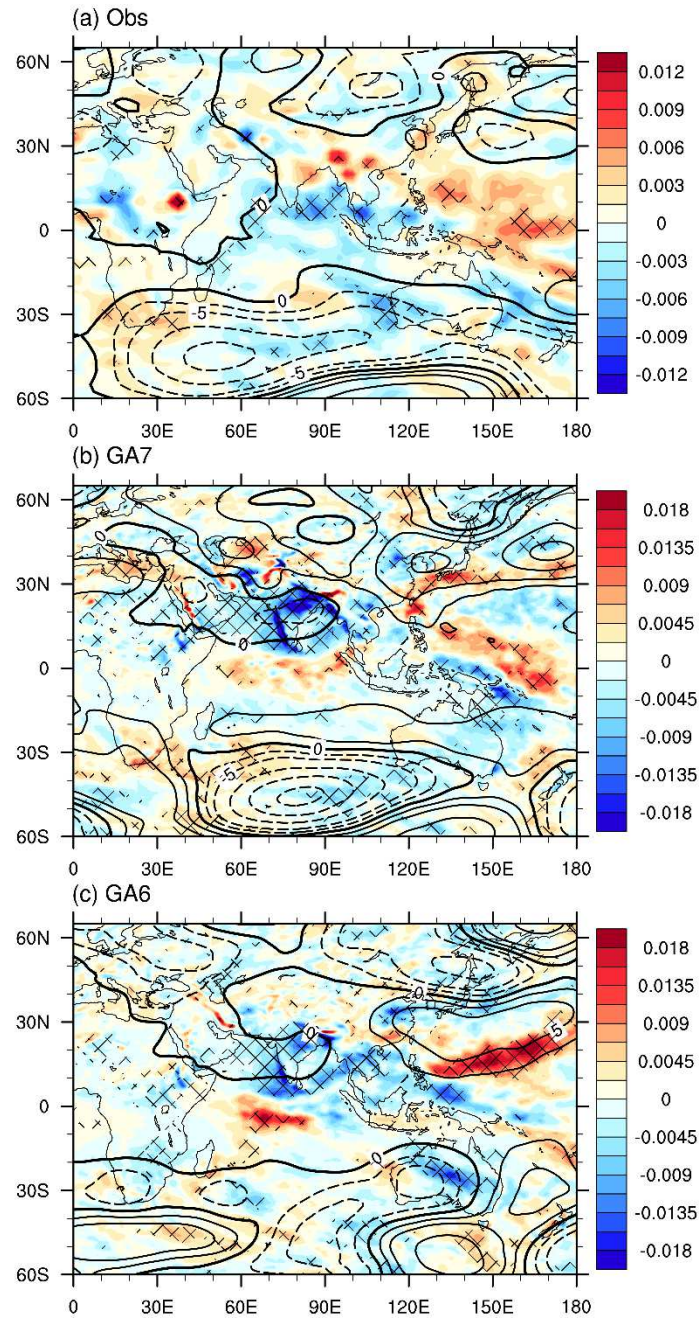
842

843 Fig. 2. Composites of strong/weak summer monsoon rainfall (JJA) for the period 1982–
 844 2008 (unit: mm day^{-1}). (a), (b) GPCP observations; (c), (d) GA6; (e), (f) GA7; and (g),
 845 (h) difference between GA7 and GA6. The black box represents the Indian summer
 846 monsoon domain. Cross hatched areas denote significance at the 90% confidence level.
 847 Strong (weak) monsoon years are determined based on when the ISMRI (normalized
 848 area-averaged summer rainfall anomalies over $70^{\circ}\text{--}90^{\circ}\text{E}$, $5^{\circ}\text{--}25^{\circ}\text{N}$) is above (below)
 849 0.75 (-0.75).



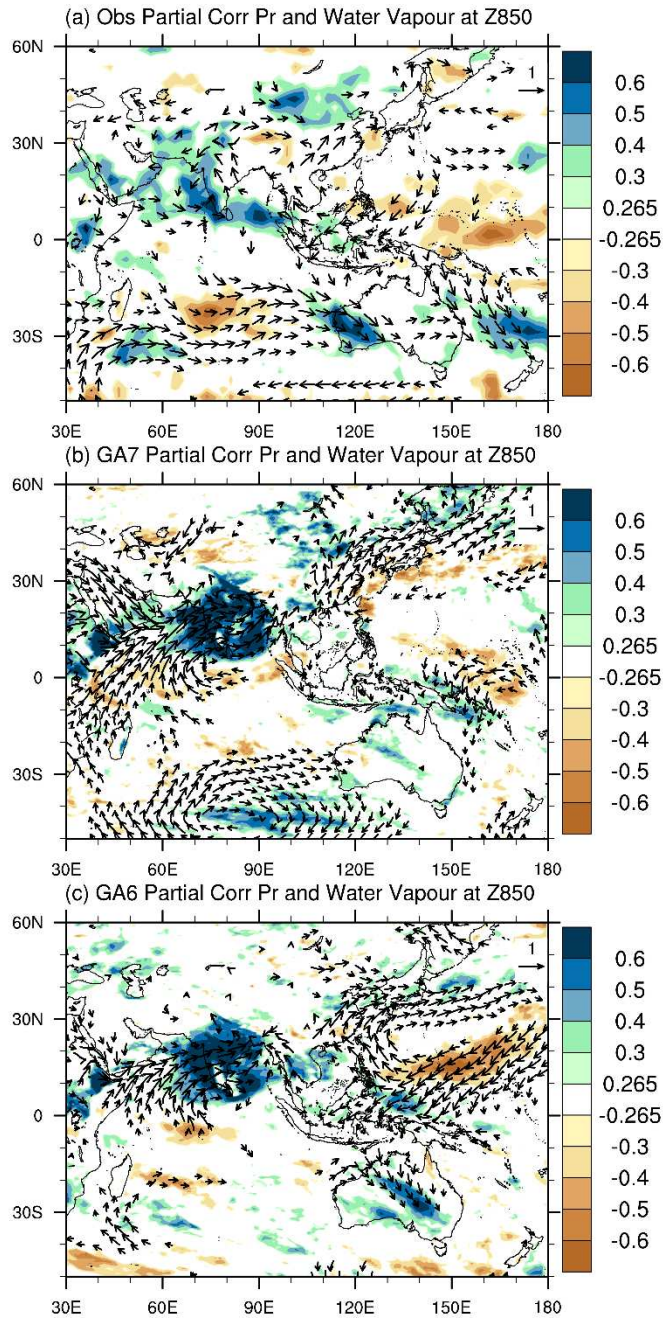
850

851 Fig. 3. Map of regression of stream function (shading; units: $\text{m}^2 \text{s}^{-1}$) and anomalous
 852 wind (vectors; units: m s^{-1}) at 500 hPa onto ISMRI (a) ERA-Interim; (c) GA7; (e) GA6.
 853 (b), (d), (f) Same as (a), (c), (e), respectively, but for partial regression excluding the
 854 signals of both ENSO and IOD. Dotted areas denote significance at the 95% confidence
 855 level; only vectors significant at the 95% confidence level are shown.



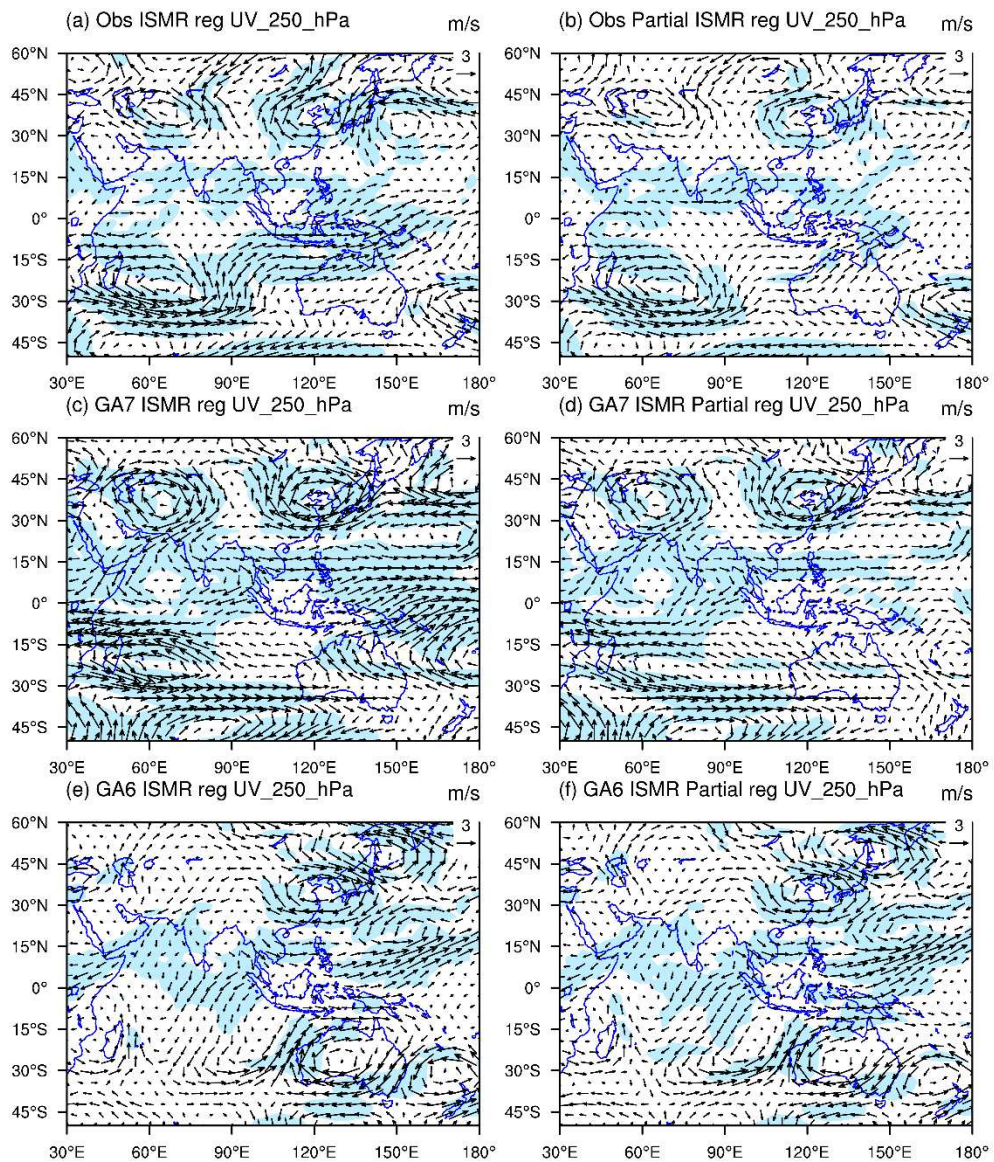
856

857 Fig. 4. Map of the partial regression of vertical velocity (shading; units: m s^{-1}) and
 858 geopotential height anomalies (contour; units: m) at 500 hPa onto ISMRI excluding the
 859 liner effects of ENSO and IOD (a) ERA-Interim; (b) GA7; (c) GA6. Thick solid lines
 860 indicate the zero lines. Cross hatched areas denote significance at the 90% confidence
 861 level.



862

863 Fig. 5. Partial correlation map of JJA rainfall (shading; units: mm) and moisture flux at
 864 850 hPa (vectors; units: mm) with ISMRI excluding the signals of ENSO and IOD (a)
 865 GPCP; (b) GA7; (c) GA6. Only shading and vectors significant at the 90% confidence
 866 level are shown.



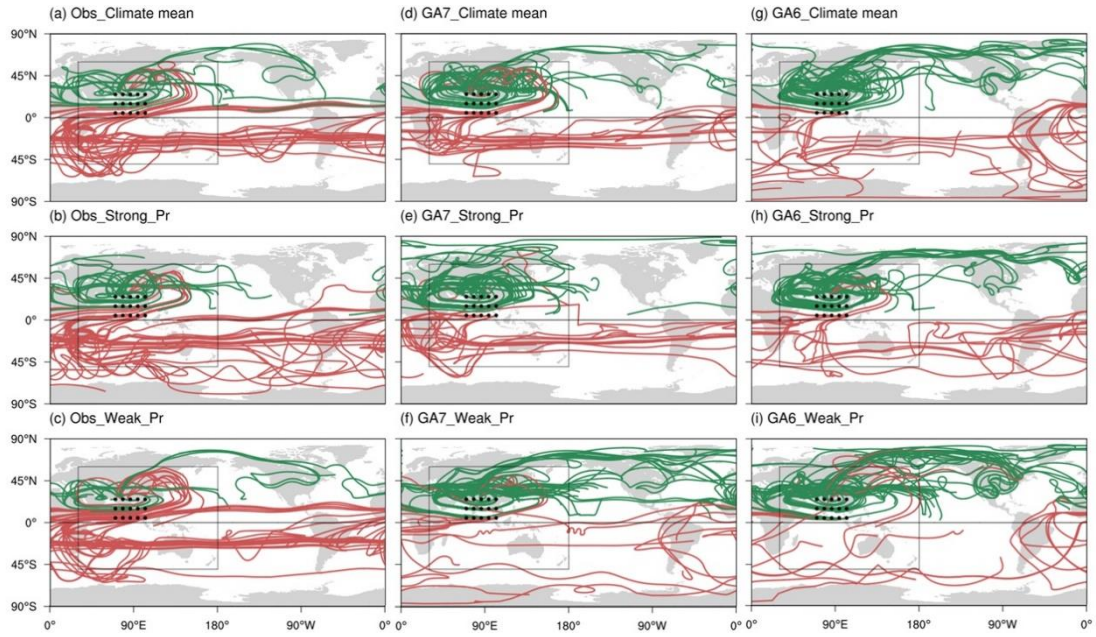
867

868 Fig. 6. Map of regression of anomalous horizontal wind (vectors; units: m s^{-1}) at 250

869 hPa onto ISMRI (a) ERA-Interim; (c) GA7; (e) GA6. (b), (d), (f) Same as (a), (c), (e),

870 respectively, but for partial regression excluding the linear influence of ENSO and IOD.

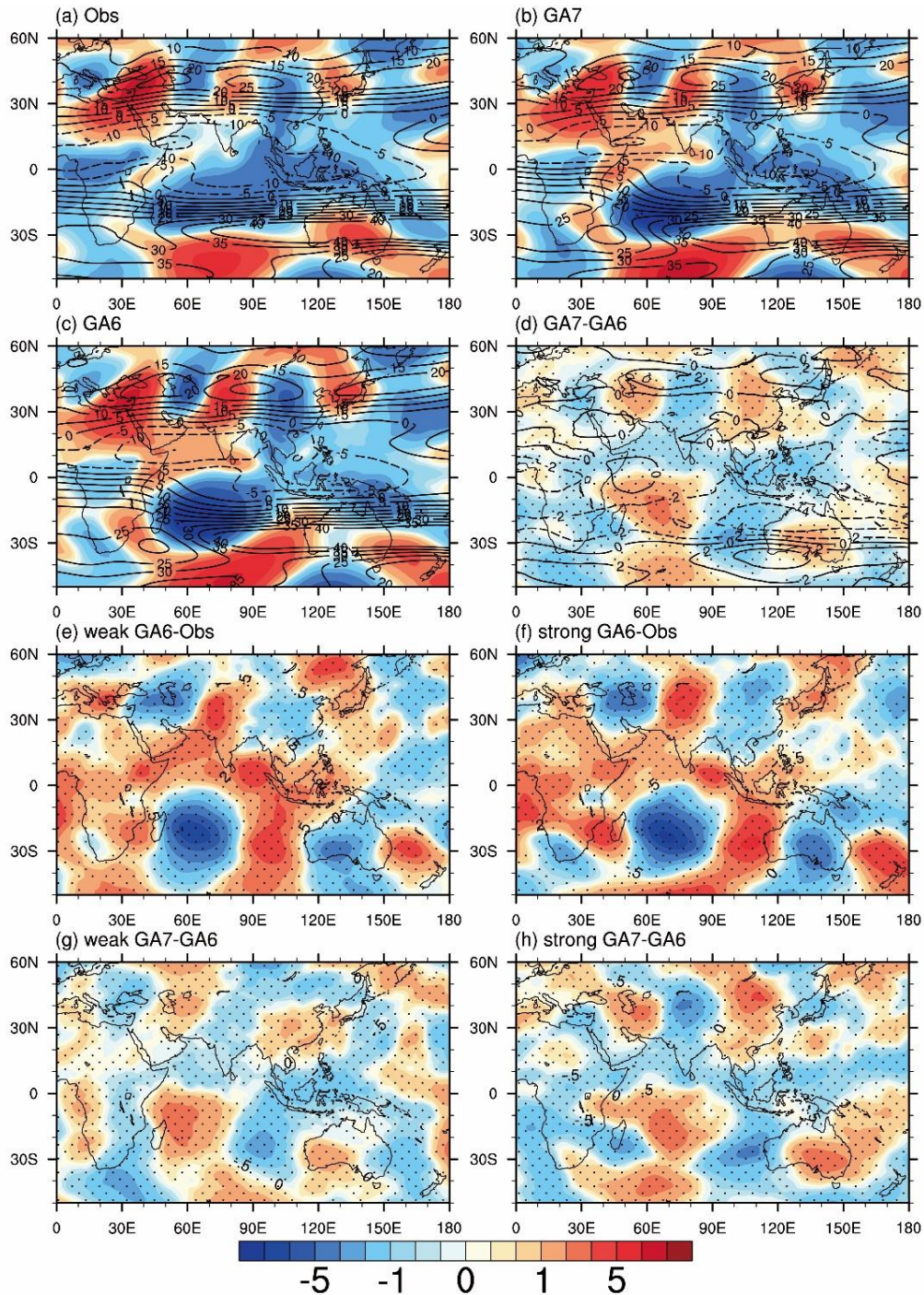
871 Shaded areas denote significance at the 90% confidence level.



872

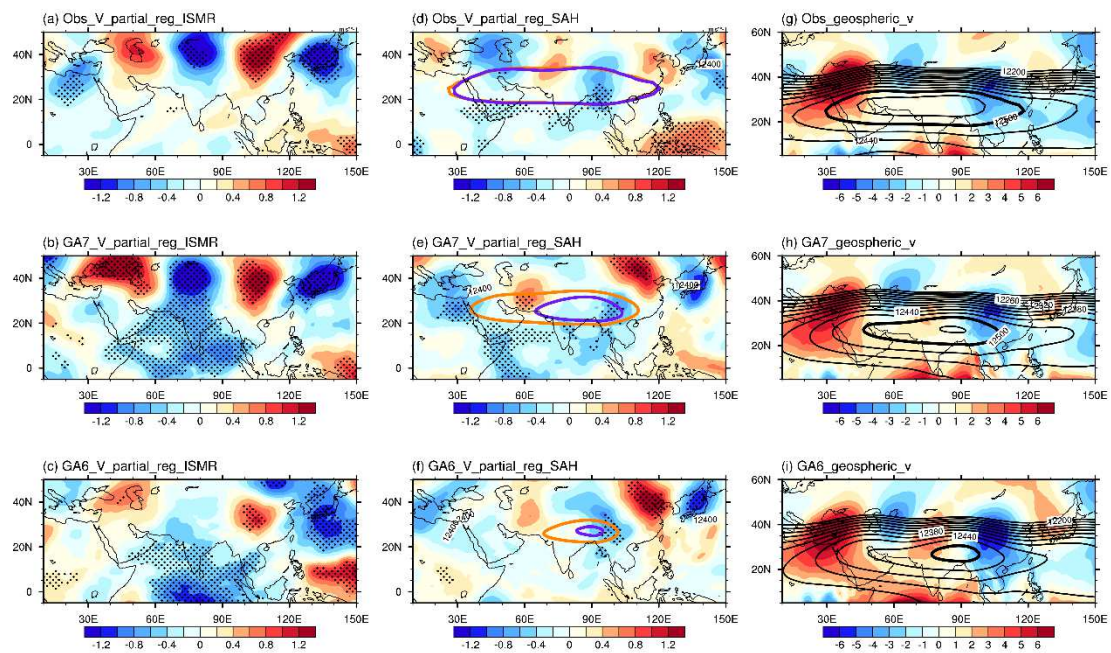
873 Fig. 7. Stationary Rossby wave ray trajectories (curves) initiated with zonal
 874 wavenumbers 2–5 from ISMR sources (black dots), driven by the 250 hPa horizontal
 875 wind, and excluding the influence of ENSO and the IOD. (a)–(c) ERA-Interim wind
 876 data; (d)–(f) GA6; and (g)–(i) GA7. Red and green curves represent the stationary
 877 Rossby waves propagating in the Southern and Northern Hemisphere, respectively.

878



879

880 Fig. 8. 250 hPa climatological zonal winds (contours; unit: m s^{-1}) and meridional winds
 881 (shading; unit: m s^{-1}) excluding the influence of ENSO and the IOD. (a) ERA-Interim;
 882 (b) GA7; (c) GA6; (d) difference between GA7 and GA6. Difference between GA6 and
 883 observations of composite meridional winds from years of (e) weak and (f) strong
 884 ISMR. Difference between GA7 and GA6 of composite meridional winds from years
 885 of (g) weak and (h) strong ISMR. Dotted areas represent significance at the 90%
 886 confidence level.



887

888 Fig. 9. Multiple regression of 200 hPa meridional wind to (a)–(c) ISMRI and (d)–(f)
 889 SAHI. (g)–(i) Meridional geospheric wind (shading; units: m s^{-1}) and geopotential
 890 height (contour; units: m). The solid lines in (g)–(i) represent the location of the
 891 climatological SAH, and the yellow and purple thick solid lines in (d)–(f) indicate the
 892 composites location of SAH in the years of strong and weak ISMR. Top column is for
 893 ERA-Interim, middle column is for GA7, and bottom column is for GA6.